water

Article

Hydrogeochemical Characteristics of Geothermal Water in Ancient Deeply Buried Hills in the Northern Jizhong Depression, Bohai Bay Basin, China

Mingxiao Yu [1,2], Xia Tian [1,3,*], Hanxiong Zhang [1,2], Jun Li [4], Laibin Wang [4], Zhigang Zhang [4], Hailiang Lin [5] and Xinlong Yang [6]

1 Institute of Hydrogeology and Environmental Geology, Chinese Academy of Geological Sciences, Shijiazhuang 050061, China; yumingxiao@mail.cgs.gov.cn (M.Y.); zhanghx1016@163.com (H.Z.)
2 Innovation Center of Geothermal and Dry Hot Rock Exploration and Development Technology, Ministry of Natural Resources, Shijiazhuang 050800, China
3 Key Laboratory of Groundwater Contamination and Remediation, China Geological Survey (CGS) & Hebei Province, Shijiazhuang 050061, China
4 Hebei Institute of Geothermal Resources Development, Hengshui 053000, China; 13932845954@163.com (J.L.); hbwlb1987@163.com (L.W.); 13932826434@163.com (Z.Z.)
5 Beijing Institute of Geothermal Investigation and Research, Beijing 102218, China; linhailiang@sohu.com
6 Beijing Huaqing Geothermal Development Group Co., Ltd., Beijing 102218, China; yangxinlong1106@163.com
* Correspondence: tianxia429@126.com

Abstract: The Jizhong Depression boasts rich geothermal resources with a lengthy history of geothermal exploitation. Buried hill geothermal reservoirs, which serve as primary thermal sources for hydrothermal resource exploitation, are prevalent in this region and have advantages such as extensive development potential, significant geothermal reservoir capacity, superior water quality, and straightforward recharge. This study investigates the formation and evolution of deep geothermal water in the Jizhong Depression by analyzing the hydrochemical and isotopic data of geothermal water samples collected from buried hill geothermal reservoirs in the northern part of the depression. The findings reveal that the subsurface hot water samples from the carbonate geothermal reservoirs in this region were predominantly weakly alkaline water with a pH ranging between 6.61 and 8.87. The hot water samples collected at the wellhead exhibited temperatures varying from 33.9 °C to 123.4 °C and total dissolved solids (TDS) lying between 473.9 mg/L and 3452 mg/L. Based on the δ^2H-$\delta^{18}O$ stable isotope analysis, the geothermal fluids in the Jizhong Depression are predominantly sourced from atmospheric precipitation and exist in a somewhat isolated hydrogeological environment, exhibiting pronounced water–rock interactions and deep water circulation (with depths ranging from 1324 m to 3455 m). Through a comparison of various methods, it is deduced that the most appropriate geothermometer for deep karst geothermal reservoirs in the Jizhong Depression is a chalcedony geothermometer, and when using it, the deep reservoir temperature was estimated at 63–137.6 °C. The precipitation in the adjacent mountainous areas enables the groundwater to infiltrate and descend deep into the earth along piedmont faults. Subsequently, lateral runoff over extended periods replenishes the groundwater into the depression. This process allows for the groundwater to fully absorb heat from deep heat sources, resulting in the formation of the deep geothermal reservoirs in the northern Jizhong Depression. The insights obtained from this study offer a theoretical and scientific foundation for the exploitation and utilization of regional geothermal resources and the transformation of the energy structure in China.

Keywords: Jizhong Depression; ancient buried hill; hydrogeochemistry; hydrogen–oxygen isotopes; geothermal reservoir temperature

check for updates

Citation: Yu, M.; Tian, X.; Zhang, H.; Li, J.; Wang, L.; Zhang, Z.; Lin, H.; Yang, X. Hydrogeochemical Characteristics of Geothermal Water in Ancient Deeply Buried Hills in the Northern Jizhong Depression, Bohai Bay Basin, China. *Water* **2023**, *15*, 3881. https://doi.org/10.3390/w15223881

Academic Editor: Paolo Madonia

Received: 28 September 2023
Revised: 21 October 2023
Accepted: 2 November 2023
Published: 7 November 2023

1. Introduction

Energy is foundational and propels the advancement of human civilization [1,2]. Currently, China stands as the world's largest energy consumer, and its energy structure is characterized by fossil energy and a large-scale energy system, among others [3]. Consequently, China faces significant challenges in maintaining its current situation and developmental trend of energy security [4–7]. In September 2020, President Xi Jinping announced a pivotal strategy for achieving peak carbon dioxide emissions by 2030 and carbon neutrality by 2060. This strategy represents China's approach to combating climate change, fostering green transitions, and ensuring energy security. Geothermal energy, epitomizing green, low-carbon, renewable energy, offers manageable and sustainable extraction. Its utilization is instrumental in reshaping the energy structure, advancing energy conservation and emission reduction, and enhancing environmental quality. Therefore, geothermal energy serves as a critical pillar for China's energy security [8]. It is projected that China's recoverable hydrothermal resources is equal to approximately 1.865 billion tons of coal, highlighting considerable exploitation potential [9]. The ancient buried hill-type geothermal reservoirs that are prevalent in North China, which are pivotal for hydrothermal geothermal exploitation, constitute roughly 70–80% of China's total hydrothermal geothermal resources. Consequently, the expansive exploration and harnessing of this type of geothermal reservoir have emerged as primary focal points in China's recent geothermal resource initiatives.

The Jizhong Depression is located in the northwest of the Bohai Bay Basin, with abundant geothermal resources and many years of geothermal development history. Carbonate thermal reservoirs distributed in this area generally have the advantages of a large development scale, large thermal storage capacity, high quality of water, and easy recharge [10–12]. In recent years, geochemical methods such as hydrochemistry and isotope have had unique advantages in revealing the recharge source of geothermal water [13–18], deducing the water–rock reaction process, and discussing the formation mechanism of geothermal water. Many scholars have used geochemical methods to study the recharge sources, thermal storage temperature, and groundwater mixing in the Jizhong Depression (such as the Xiong'an New Area) [19–22]. However, the whole region lacks systematic and comprehensive research. On the basis of collecting previous research results, this paper selects the northern part of the Jizhong Depression as the research object and analyzes the characteristics of the hydrochemical components. Combined with the water supply of the underground hot water, the thermal storage temperatures were estimated by using a geochemical temperature scale, a multi-mineral balance diagram, and the silicon–enthalpy equation. This research provides a theoretical and scientific basis for the development and utilization of regional geothermal resources and the transformation of energy structure.

2. Geological Setting

The Jizhong Depression, situated in the northwest of the Bohai Bay Basin, is bordered by the Yanshan Uplift to the north, the Xingheng Uplift to the south, the Taihangshan Uplift to the west, and the Cangxian Uplift to the east, stretching in a northeast orientation [23] (Figure 1a). Regionally, the Jizhong Depression has undergone multiple tectonic phases, resulting in a concave–convex structural pattern. It is segmented into southern, central, and northern zones by two transform zones: the nearly WE Wuji-Hengshui zone and the NWW Xushui-Anxin-Wenan zone [24]. This study focuses on the northern Jizhong Depression, encompassing six fourth-order tectonic units, namely the Beijing, Dachang, and Langgu depressions, as well as the Daxing, Niutuozhen, and Rongcheng uplifts. Faults are distributed in the study area, exhibiting an NE trend overall and predominantly including extensional faults such as the Taihang Mountains piedmont, Tongxian-Nanyuan, Daxing, Rongcheng, Rongdong, and Niudong faults from the northwest to southeast (Figure 1b). These faults significantly influence the distribution of regional secondary tectonic units. The Daxing fault, with its varied orientation, exhibits distinct geological and tectonic characteristics in different segments [25]. Specifically, its northern segment has an NNE strike and is connected to the boundary fault that dictates the Dachang Depression to the north; its middle segment has a NE strike, governing the boundary between the Daxing Uplift and the Langgu Depression; and its southern segment has varied orientations, reflecting the variability of the fault activity. The Rongcheng fault, which extends to the crystalline basement, is a growth fault influencing the development of Neoproterozoic strata [26]. The Rongdong fault with a strike of NNE delineates the boundary between the Niutuozhen and Rongcheng uplifts. The Niudong fault impacts both the Niutuozhen Uplift and the Baxian Depression, serving as a deep-seated, long-term active fault penetrating the crystalline basement [27]. Collectively, these faults shape the regional tectonic framework and play pivotal roles in geothermal resource formation by acting as thermal and water conduits. Additionally, predominant deposits in the study area comprise Archean metamorphic rock, Upper-Middle Proterozoic carbonate rock, Ordovician–Cambrian, Neogene sandstone, and Quaternary sediment from bottom to top [28]. The Cenozoic cover primarily consists of sandstone, mudstone, and sandy mudstone. The primary geothermal reservoirs are mainly carbonate rocks, with the top interface influenced by regional basement tectonics and the lithology characterized by gray dolomite and muddy dolomite [23]. The rock fissures, due to their advanced development and superior thermal properties, underscore the Jizhong Depression's geothermal resource potential.

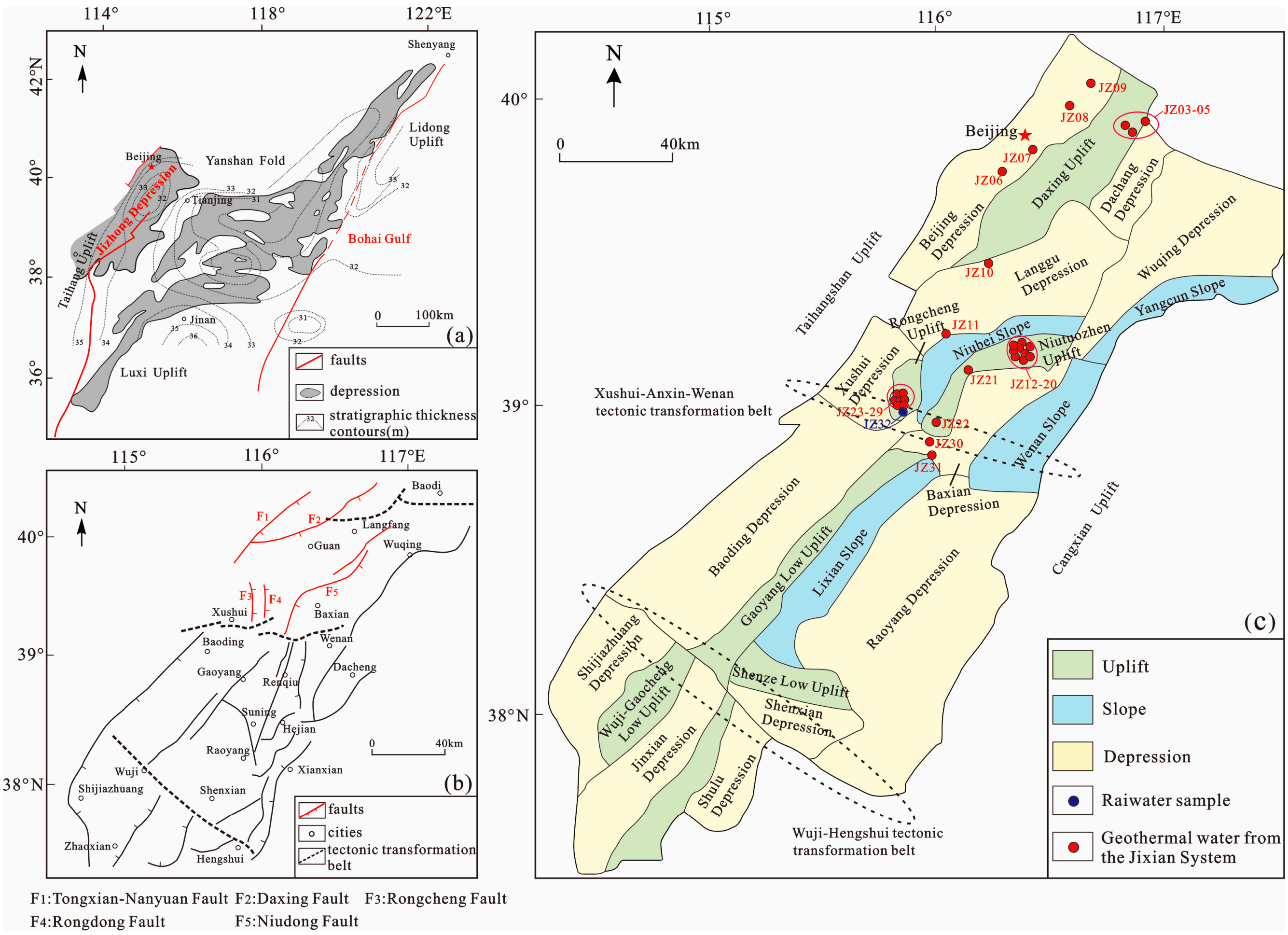

Figure 1. (**a**) Tectonic units of Bohai Bay Basin. (**b**) Distribution map of faults in the Jizhong Depression. (**c**) Distribution map of geothermal fluids in the study area (modified from [28,29]).

3. Material and Methods

In this study, 25 groups of water samples and an additional 7 groups were collected, totaling 32 groups. The distribution of samples across tectonic units is as follows: three from the Daxing Uplift, four from the Beijing Depression, two from the Langgu Depression, eleven from the Niutuozhen Uplift, seven from the Rongcheng Uplift, two from the Gaoyang Low Uplift, one from local rainfall, and two from the Taihang Mountains' mountainous areas (Figure 1c). During field sample collection from geothermal wells, the geographic locations, coordinates, and geological structures of the sample sites were recorded. Furthermore, the water temperature at wellhead was gauged using an infrared geothermometer, while pH, oxidation–reduction potential (ORP), and TDS were measured using a multi-parameter water quality analyzer. The water samples were collected into thrice-cleaned 500 mL volumetric flasks, sealed for preservation, and then dispatched to the Key Laboratory of Groundwater Science and Engineering, Ministry of Land and Resources for comprehensive hydrochemical analysis. Cation concentrations in the samples were detected via the ICP-AES (Inductively Coupled Plasma Atomic Emission Spectrometry) method, while anions were assessed using the ion chromatography method (Dionex-500), ensuring an accuracy of 0.02 mg/L for both anions and cations and an equilibrium error below 5%. SiO_2 (dissolved) was gauged via spectrophotometry. The δ^2H and $\delta^{18}O$ values were determined as per the DZ/T 0184.19-1997 standard [30], using a water isotope analyzer (Picarro2140-i), with detection accuracies of 0.1 and 0.3, respectively, and the analytical error was maintained at ±0.5%. The chemical composition results of hot water samples from the underground carbonate geothermal reservoirs in the study area are detailed in Table 1.

Table 1. Hydrochemical analysis data of the geothermal water from different aquifers in the study area (mg/L).

Sample No.	Station	Longitude	Latitude	T (°C)	TDS	pH	K^+	Na^+	Ca^{2+}	Mg^{2+}
JZ01 *	Taihang Mountains	115°12′35.04″	39°04′13.37″	14.0	458	7.69	0.7	9.02	70.6	25.2
JZ02 *	Taihang Mountains	115°47′36.9″	39°19′51.1″	14.0	501.9	7.92	2.3	15.6	80.8	23.5
JZ03	Daxing Uplift	116°46′55″	39°55′02″	33.9	619.6	8.37	19	136.5	8.7	18.7
JZ04	Daxing Uplift	116°57′40″	40°00′02″	59.2	675.8	7.93	24.7	128	28.6	12.5
JZ05	Daxing Uplift	116°47′57″	39°53′21″	37.9	670.2	7.85	19.3	153.5	13.4	9.6
JZ06 *	Beijing Depression	/	/	36.4	498.4	8.2	9.5	57.1	67.4	23.5
JZ07 *	Beijing Depression	/	/	67.0	473.9	7.9	9.2	74.9	46.7	19.9
JZ08 *	Beijing Depression	/	/	45	711	8.2	18.6	177.5	39.3	14.4
JZ09 *	Beijing Depression	/	/	58	1520	8.3	36.3	533.8	13.2	5.7
JZ10	Langgu Depression	116°12′44″	39°29′05″	74.4	3076	7.24	54.6	954.4	41.9	22.6
JZ11	Langgu Depression	116°03′53″	39°07′03″	82	3267.4	7.64	55.1	1019	40.8	24.8
JZ12	Niutuozhen Uplift	116°21′47″	39°14′51″	86	2940	7.13	55.6	970	43.7	26.5
JZ13	Niutuozhen Uplift	116°19′59″	39°12′34″	86	2842	7.57	50.6	915.9	41.6	21.7
JZ14	Niutuozhen Uplift	116°16′35″	39°13′42″	80	2971.9	7.61	53.6	958.7	47.3	24.8
JZ15	Niutuozhen Uplift	116°17′12″	39°13′47″	80	2899.3	7.15	51.3	950.1	50	22.6
JZ16	Niutuozhen Uplift	116°20′15″	39°13′12″	88	2958	7.42	56.1	934.4	41.9	19.3
JZ17	Niutuozhen Uplift	116°19′47″	39°13′14″	91	2871	7.5	53.8	851.1	47.5	22.2
JZ18	Niutuozhen Uplift	116°17′41″	39°14′08″	81	3137.2	7.6	52.5	989.5	71.4	36.1
JZ19	Niutuozhen Uplift	116°20′38″	39°13′39″	87	3044	7.31	51	933.2	42.4	21
JZ20	Niutuozhen Uplift	116°21′54″	39°15′08″	85	2787.6	8.2	51.6	855	49	23
JZ21	Niutuozhen Uplift	116°11′41″	39°08′40″	83	2991	7.3	54.8	914.3	48.1	23.3
JZ22	Niutuozhen Uplift	116°01′12″	38°56′15″	84	/	7.34	47.3	831.9	39.6	23.7
JZ23	Rongcheng Uplift	115°50′55″	39°03′08″	55	2881	7.61	44.6	841.5	65.6	30.4
JZ24	Rongcheng Uplift	115°52′53″	39°02′56″	50	2505	7.33	50.5	844.5	63	38.8
JZ25	Rongcheng Uplift	115°51′22″	39°02′42″	52	2734	8.87	41.1	800.3	62	31.5
JZ26	Rongcheng Uplift	116°55′03″	39°03′19″	53.1	3452	6.61	43	839.5	176.9	85.4
JZ27	Rongcheng Uplift	115°51′45.00″	38°59′07.59″	72	2787	7.4	43.2	782.6	55.4	29
JZ28	Rongcheng Uplift	115°52′59.11″	39°00′55.24″	62	2914	7.1	47	827.1	62.6	32

Table 1. *Cont.*

Sample No.	Station	Longitude	Latitude	T (°C)	TDS	pH	K^+	Na^+	Ca^{2+}	Mg^{2+}
JZ29	Rongcheng Uplift	115°52′40.63″	39°05′29.03″	70.8	2704	7.32	41.8	774.3	48.9	26
JZ30	Gaoyang Low Uplift	115°56′37.91″	38°52′22.24″	109.2	2606	7.94	47.8	769.2	35.5	9.1
JZ31	Gaoyang Low Uplift	115°57′24″	38°47′09″	123.4	2980	8.48	64	920.6	17	4.3
JZ32 *	Rain Sample	115°55′42.36″	38°58′39.22″	20	26.88	7.85	1.2	4.4	54.3	19
Sample No.	**Station**	**Li^+**	**Sr^{2+}**	**HCO_3^-**	**Cl^-**	**SO_4^{2-}**	**SiO_2**	**F^-**	**Hydrochemical Type**	
JZ01 *	Taihang Mountains	/	0.1	276.5	11.32	17	/	/	HCO_3-Ca·Mg	
JZ02 *	Taihang Mountains	/	0.38	261.1	17.95	68.1	/	/	HCO_3-Ca·Mg	
JZ03	Daxing Uplift	0.36	0.17	310.6	50.9	22.1	21.6	19.2	HCO_3-Na·Mg	
JZ04	Daxing Uplift	0.34	0.23	366	45.3	40.5	22.4	7.9	HCO_3-Na	
JZ05	Daxing Uplift	0.43	0.3	300.8	63.7	72.2	20.1	14.3	HCO_3·Cl-Na	
JZ06 *	Beijing Depression	0.15	1.89	271.5	33.5	133.8	73.4	4.7	HCO_3·SO_4-Ca·Na·Mg	
JZ07 *	Beijing Depression	0.19	0.96	213.6	47.5	110.7	61.8	4.8	HCO_3·SO_4-Na·Ca·Mg	
JZ08 *	Beijing Depression	0.3	1.14	348.4	105.5	129.8	58.9	7.2	HCO_3·Cl·SO_4-Na	
JZ09 *	Beijing Depression	0.76	0.88	774.9	394.7	36.8	63.2	13.4	HCO_3·Cl-Na	
JZ10	Langgu Depression	1.97	1.89	529.4	1345	14.83	72.9	9.8	Cl-Na	
JZ11	Langgu Depression	/	/	530.9	1453.4	90.9	68.8	11.6	Cl-Na	
JZ12	Niutuozhen Uplift	1.51	1.65	476	1350	7.7	73.6	10	Cl-Na	
JZ13	Niutuozhen Uplift	1.31	1.48	479.2	1215	8.58	57.7	17	Cl-Na	
JZ14	Niutuozhen Uplift	1.85	1.66	488.1	1318.9	6	68.5	8.1	Cl-Na	
JZ15	Niutuozhen Uplift	1.91	1.62	457.4	1289.3	4.8	60.5	9.7	Cl-Na	
JZ16	Niutuozhen Uplift	1.72	1.69	481.5	1296	10	63.7	9.6	Cl-Na	
JZ17	Niutuozhen Uplift	1.64	1.73	492.5	1288	6	57.9	10	Cl-Na	
JZ18	Niutuozhen Uplift	1.87	1.6	452.3	1457	10.1	60.3	10.1	Cl-Na	
JZ19	Niutuozhen Uplift	1.91	1.86	466	1418	3.89	60.2	9.5	Cl-Na	
JZ20	Niutuozhen Uplift	1.61	1.47	472.4	1259.3	4	52.5	10	Cl-Na	
JZ21	Niutuozhen Uplift	1.24	1.94	505.2	1375.6	3.9	46.9	2.1	Cl-Na	
JZ22	Niutuozhen Uplift	/	/	482.1	1240.8	2.7	43	9.6	Cl-Na	
JZ23	Rongcheng Uplift	1.25	2.17	585	1084	40.4	107.4	8.2	Cl·HCO_3-Na	
JZ24	Rongcheng Uplift	1.32	1.3	702.43	1095.4	14.1	150.3	7.5	Cl·HCO_3-Na	
JZ25	Rongcheng Uplift	1.21	1.62	618.8	1033	24	28.4	8	Cl·HCO_3-Na	
JZ26	Rongcheng Uplift	1.35	2.3	699.8	1450	43	50.2	7.3	Cl·HCO_3-Na	
JZ27	Rongcheng Uplift	1.56	/	704.3	1085	2.2	34.4	7.4	Cl·HCO_3-Na	
JZ28	Rongcheng Uplift	1.41	2.65	735	1118	4.2	41.6	6.5	Cl·HCO_3-Na	
JZ29	Rongcheng Uplift	1.36	2.51	645.2	1076	4.1	40.9	7.6	Cl·HCO_3-Na	
JZ30	Gaoyang Low Uplift	1.33	2.57	540.7	1041	12.8	46.3	7.3	Cl·HCO_3-Na	
JZ31	Gaoyang Low Uplift	1.75	2.32	448.7	1271	5.4	46.4	11.1	Cl-Na	
JZ32 *	Rain Sample	/	0.15	17.9	1.74	1.6	21.6	/	HCO_3-Ca·Mg	

Note: "*" indicates the data collected from [21,31].

4. Results and Discussion

4.1. Hydrochemistry

The Aquachem software (V 4.0) [32] was utilized to plot Piper trilinear diagrams for the water sample locations (Figure 2). Based on these diagrams and the hydrochemical test results (Table 1) [33,34], it can be determined that the spring water in the zone with exposed carbonate rocks in the Taihang Mountains' mountainous area has an average temperature of 14 °C, a pH of 7.69–7.92, a TDS between 458 and 501.9 mg/L, and a hydrochemical type of HCO_3-Ca·Mg. Carbonate reservoirs primarily comprise thickly laminated dolomite, with carbonate minerals such as calcite and dolomite serving as the primary sources of Ca^{2+}, Mg^{2+}, and HCO_3^- [35]. A total of 29 geothermal water samples from the study area's carbonate reservoirs were mostly weakly alkaline, with a pH ranging from 6.61 to 8.87, with an average of 7.7. The hot water samples collected at the wellhead exhibited temperatures spanning from 33.9 to 123.4 °C, a TDS from 473.9 to 3452 mg/L, and a dissolved SiO_2 content ranging from 20.08 to 150.31 mg/L. The samples from both the Daxing Uplift and the Beijing Depression displayed diverse hydrochemical types, predominantly comprising Na·Mg-HCO_3, Ca·Na·Mg-HCO_3·SO_4, Na·Ca·Mg-HCO_3·SO_4, and Na-HCO_3·Cl·SO_4. In contrast, the water samples from the Langgu Depression, Niutuozhen Uplift, Rongcheng Uplift, and Gaoyang Low Uplift primarily showed two hydrochemical types: Na-Cl and Na-Cl-HCO_3.

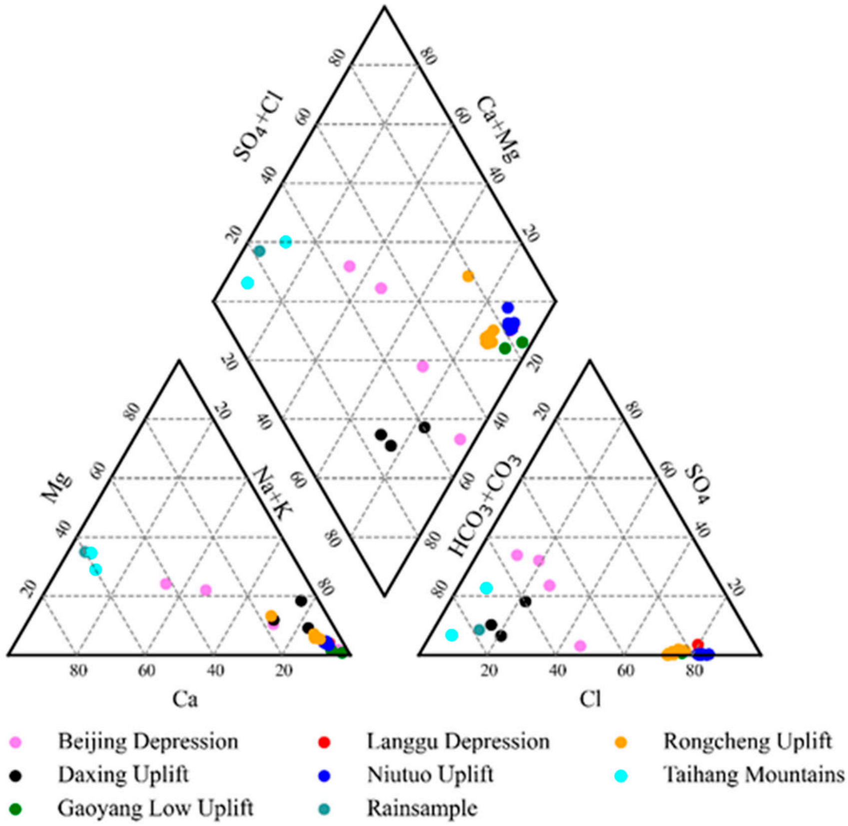

Figure 2. Geothermal fluid Piper trilinear diagram.

Comparing the water sample data from the Taihang Mountains, Daxing Uplift, Beijing Depression, Langgu Depression, Niutuozhen Uplift, Rongcheng Uplift, and Gaoyang Low Uplift, there is a sequential increase in the groundwater TDS from the recharge zone to the runoff zone and then to the discharge zone. Accordingly, the hydrochemical type changes, with the Na^+ cation becoming gradually predominant. Water–rock interactions cause Mg^{2+} and Ca^{2+} in the geothermal water to replace Na^+ in the surrounding minerals and then be adsorbed by the reservoir rock. The HCO_3^- and Cl^- contents increase progressively (Figure 3). Among them, HCO_3^- originates from the dissolution and filtration of carbonate minerals, while Cl^- exhibits significant migration and solubility [20]. The decreasing SO_4^{2-} content from the recharge to discharge areas suggests the gradual closing of the geothermal water space and a shift from an oxidizing to a reducing environment, with desulfurization leading to H_2S production (Figure 4).

In the study area, the Li^+ concentrations in the water samples ranged from 0.151 to 1.97 mg/L. As per GB8537-2018 [36], all water samples met the criteria for lithium mineral water, except for the JZ06 and 07 samples. The Sr^{2+} concentration in the samples spanned from 0.296 to 2.692 mg/L, fulfilling the criteria for strontium mineral water. The F^- concentrations varied between 4.65 and 19.22 mg/L. The high fluoride concentration in the underground hot water is primarily ascribed to the weakly alkaline environment, water temperature, and water–rock interactions.

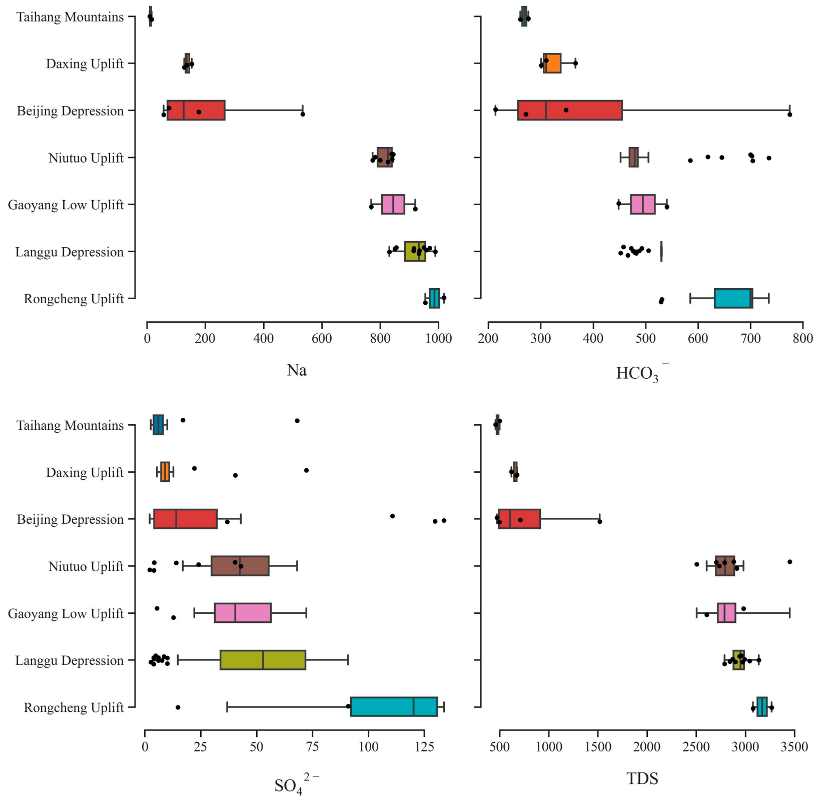

Figure 3. Diagram of anion and cation content of geothermal fluids in the study area.

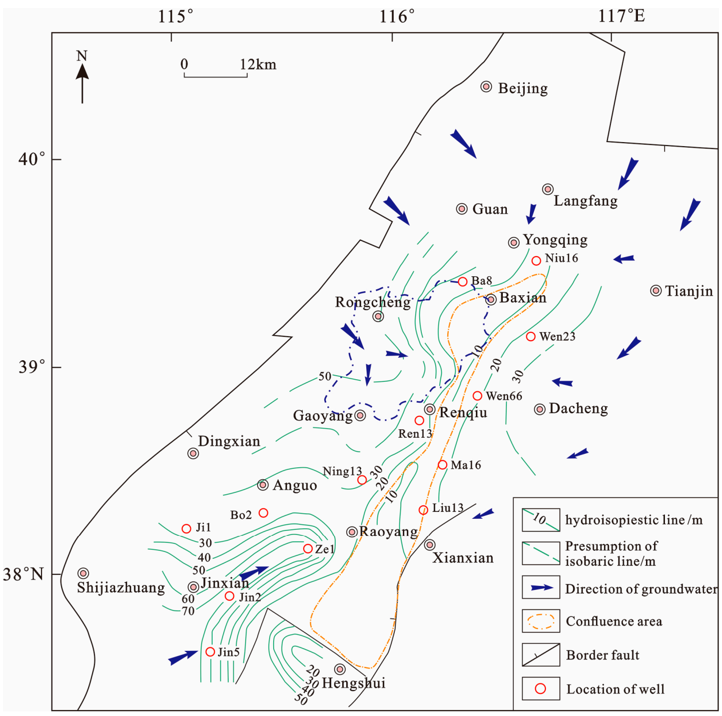

Figure 4. Contour map of the phreatic pressure level elevation in the Jizhong Depression [37].

4.2. Isotopic Composition of Water

Studying the isotope characteristics of groundwater hydroxides allows for the determination of the groundwater origins [21] and the understanding of groundwater circulation pathways based on the varied distributions of the hydroxide isotope data in the diagram

(Figure 5) showing the δ^2H-δ^{18}O relationships. In this research, the local meteoric water line (LMWL) [26] was used to plot the δ^2H and δ^{18}O values of the water samples (Table 2) on the relationship diagram. The hydroxide isotope data of the water samples from the study area roughly fell on one side of the GMWL. A strong correlation between the δ^2H and δ^{18}O values indicates that the geothermal water in the study area's paleo-submerged geothermal reservoirs is recharged by atmospheric precipitation infiltrating them (Figure 5). When compared to the Taihang Mountains and the Beijing Depression, the hydrogen and oxygen isotope data from the Niutuozhen Uplift and Rongcheng Uplift deviate more significantly from the GMWL, displaying a pronounced oxygen drift. This suggests a progressively enclosed environment and increasingly deep carbonate geothermal reservoirs from the recharge to discharge areas. Furthermore, there exist intense isotope exchanges in the regions with elevated temperatures.

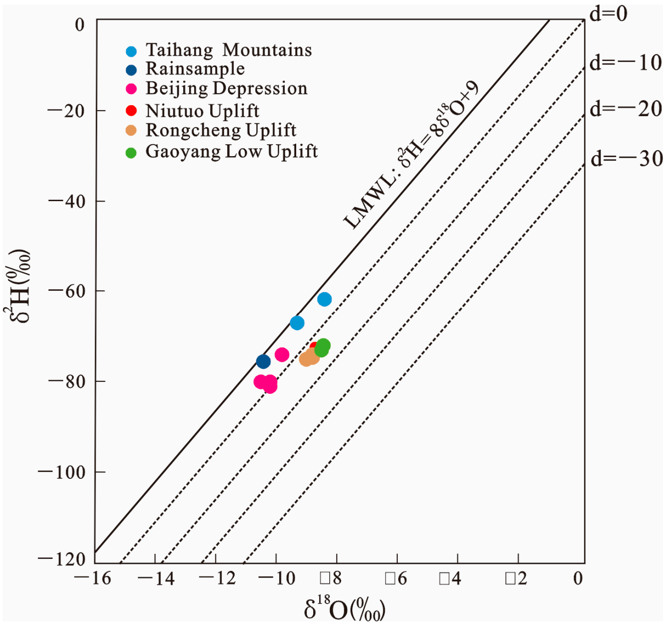

Figure 5. Plot of δ^2H (‰) and δ^{18}O (‰) of geothermal fluids in the study area.

Table 2. δ^2H (‰) and δ^{18}O (‰) isotopic data of geothermal fluids in the study area.

Sample No.	Station	δ^2H	δ^{18}O
JZ01	Taihang Mountains	−61.64	−8.4
JZ02	Taihang Mountains	−67	−9.3
JZ06 *	Beijing Depression	−74	−9.8
JZ07 *	Beijing Depression	−81	−10.2
JZ08 *	Beijing Depression	−80	−10.5
JZ09 *	Beijing Depression	−80	−10.2
JZ17	Niutuo Uplift	−73	−8.5
JZ20	Niutuo Uplift	−73	−8.6
JZ25	Rongcheng Uplift	−74.62	−8.79
JZ27	Rongcheng Uplift	−74	−8.8
JZ28	Rongcheng Uplift	−75	−9
JZ29	Rongcheng Uplift	−75	−9

Table 2. *Cont.*

Sample No.	Station	δ^2H	δ^{18}O
JZ30	Gaoyang Low Uplift	−71.99	−8.44
JZ31	Gaoyang Low Uplift	−73	−8.5
JZ32	Rain Sample	−75	−10.5

Note: "*" indicates the data collected from [22].

4.3. Geothermal Reservoir Temperature Estimation

The geothermal reservoir temperature is crucial for understanding the geothermal activity. This temperature serves as a fundamental basis for categorizing the genetic type of geothermal resources, assessing resource potential, and choosing the appropriate exploitation and utilization approach [38]. In the absence of boreholes or when boreholes fail to reach the geothermal reservoirs, geothermometry offers an avenue to estimate the temperature of deep geothermal reservoirs [39]. The current prevalent geothermometers encompass both the cationic geothermometers and the SiO_2 geothermometers. Additionally, the multi-mineral equilibrium diagram, along with the silicon–enthalpy equation method that considers cold water mixing, can address the shortcomings of geothermometers [40]. As such, they are also widely applied to the estimation of the geothermal reservoir temperature.

4.3.1. Combination of Empirical Chemical Geothermometers

Utilizing geothermometers to estimate the temperatures of a geothermal system of low- to medium-temperature carbonate geothermal reservoirs poses multiple challenges [41]. Among these are the underestimation of geothermal reservoir temperatures, the difficulties in reaching the equilibrium of hydrothermal alteration minerals in geothermal fluids, and the limitations associated with controlling hydrochemical component minerals [42]. In the current study, a range of geothermometers were first employed to predict the deep geothermal reservoir temperature in the study area (Table 3). Notably, the derived values of geothermal reservoir temperatures using these diverse methods displayed substantial variations, necessitating a comprehensive examination of the applicability of each method.

Table 3. Geothermal temperature scale formula of the hot water.

Geothermometers	Formulas	Numbers
Na-K	$T(^\circ C) = \frac{1217}{1.483 - \lg(Na/K)} - 273.15$	(1)
K-Mg	$T(^\circ C) = \frac{4410}{14.0 - \lg\left(K^2/Mg\right)} - 273.15$	(2)
Na-K-Ca	$T(^\circ C) = \frac{1647}{5.217 + \lg(Na/K) + \frac{2}{3}\lg(\sqrt{Ca}/Na)} - 273.15$	(3)
Quartz	$T(^\circ C) = -42.198 + 0.288\,31SiO_2 - 3.6686 \times 10^{-4}\,(SiO_2)^2 + 3.1665 \times 10^{-7}(SiO_2)^3 + 77.0341\lg SiO_2$	(4)
Quartz (no steam loss)	$T(^\circ C) = \frac{1309}{5.19 - \lg SiO_2} - 273.15$	(5)
Quartz (maximum steam loss)	$T(^\circ C) = \frac{1522}{5.75 - \lg SiO_2} - 273.1$	(6)
Chalcedony	$T(^\circ C) = \frac{1032}{4.69 - \lg SiO_2} - 273.1$	(7)

(According to [43–46]).

The commonly used cationic geothermometers include Na-K, Na-K-Ca, and K-Mg geothermometers [43–47]. Typically, when these cationic geothermometers are used to estimate the temperatures of deep thermal reservoirs, the Na-K-Mg triangular diagram proposed by Giggenbach (1988) [47] is frequently adopted to determine whether the geothermal fluids have reached an equilibrium state in the water–rock interactions. As illustrated in Figure 6, the water sampling points predominantly fall within the zone of immature water. This finding illuminates that the deep reservoir temperature inferred using the Na-K thermometer, which works based on the K^+-to-Na^+-concentration ratio in the geothermal fluid, was markedly elevated compared to the temperature determined through direct measurements. The K^+-to-Na^+-concentration ratio is heavily dependent on the ion exchange reactions transpiring between potassium and sodium feldspars [42]. Although the Na-K geothermometer is more applicable to the estimation of temperatures of high-temperature reservoirs, specifically those above 200 °C, it encounters challenges in achieving ion-exchange equilibrium between potassium and sodium feldspars when used to estimate temperatures of moderate- and low-temperature geothermal reservoirs (below 200 °C) [48]. This finding accounts for the pronounced deviation from the equilibrium line that is observed for a plethora of sample points from moderate- and low-temperature geothermal reservoirs. While K-Mg equilibrium is relatively easier to achieve [47], the influence of mixing could potentially skew the K-Mg geothermometer outcomes, with the computational accuracy yet to be accurately evaluated. Furthermore, the Na-K-Ca geothermometer, proposed by Fournier and Truesdell (1973) [45], originates from empirical data. Yet, when employed in the study area, its predictions were typically lower than the observed water temperatures. Collectively, these observations insinuate that utilizing cationic geothermometers to predict the temperatures of geothermal fluids in deep carbonate geothermal reservoirs in the study area might not be the most pragmatic approach.

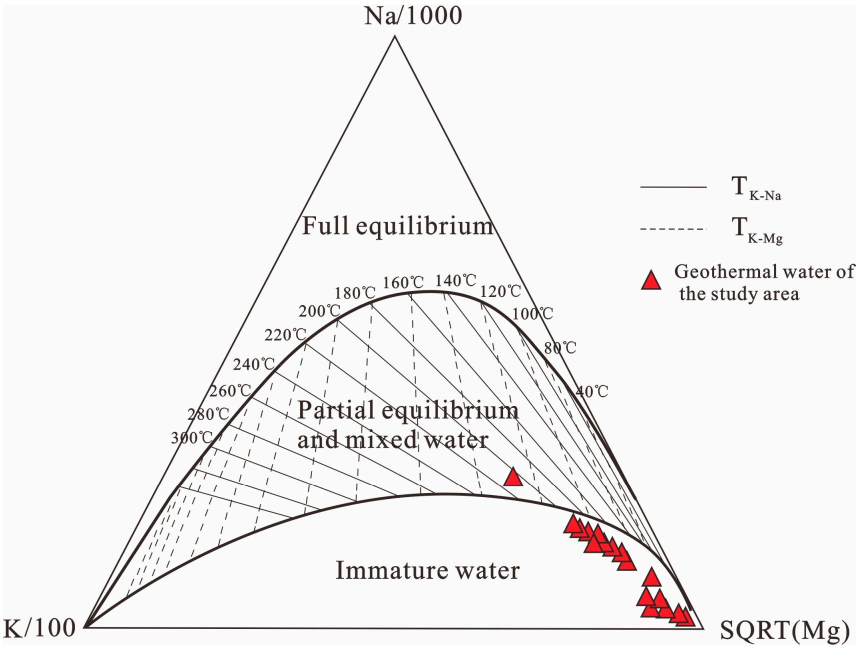

Figure 6. Diagrammatic representation of the Na-K-Mg equilibrium of geothermal fluids.

SiO_2 geothermometers are constructed upon the solubility characteristics of SiO_2 minerals. Remarkably, SiO_2 dissolved in water is relatively immune to the vagaries of ionic interactions, the evapotranspiration of other complexes, and dilution. The solubility of SiO_2 and other minerals increases with the temperature and, inversely, their precipitation accelerates when the temperature declines; therefore, different mineral contents mirror respective geothermal fluid temperatures [21]. Among the SiO_2 geothermometers that are commonly used today include quartz and chalcedony geothermometers. The analysis in this study (Table 4) suggests that the chalcedony geothermometer predictions are more aligned with the directly measured water temperatures at the wellhead. Furthermore, the research underpins the notion that in a geothermal system with a temperature below 180 °C, chalcedony, rather than quartz, is predominantly responsible for overseeing the dissolution kinetics of SiO_2 in the geothermal medium [49]. In culmination, the chalcedony geothermometer is more applicable to the study area than the quartz geothermometer, projecting the temperatures of carbonate geothermal reservoirs in the study area to range between 63 and 137.6 °C.

Table 4. Estimated temperature of the geothermal reservoir based on wellhead measurements and geothermometers.

Sample No.	Measured Water Temperatures (°C)	Cationic Geothermometers			SiO_2 Geothermometers			
		(1)	(2)	(3)	(4)	(5)	(6)	(7)
JZ07	67	238.0	56.7	29.9	112.3	112.0	111.3	82.9
JZ08	45	223.6	76.3	41.8	109.9	109.6	109.3	80.3
JZ09	58	188.3	105.8	60.3	113.4	113.1	112.3	84.1
JZ10	74.4	175.5	98.1	55.3	121.0	120.8	118.9	92.5
JZ12	86	175.6	96.4	55.3	120.8	120.6	118.7	92.3
JZ14	80	173.9	96.3	53.6	109.9	109.6	109.3	80.3
JZ15	80	171.4	96.4	52.0	113.4	113.1	112.3	84.1
JZ16	88	179.0	100.9	56.3	120.5	120.3	118.4	91.9
JZ19	87	172.2	97.1	53.5	117.4	117.1	115.7	88.5
JZ21	83	178.9	97.8	54.5	113.7	113.4	112.6	84.5
JZ23	55	170.1	88.8	46.8	99.2	98.8	100.0	68.7
JZ26	53.1	167.6	75.0	37.1	102.4	102.0	102.8	72.1
JZ28	62	175.1	89.5	48.8	93.9	93.4	95.3	63.0
JZ30	109.2	181.6	107.0	55.2	141.4	141.2	136.1	115.0
JZ31	123.4	189.9	127.0	69.3	161.6	161.3	152.9	137.6

Note: "(1)–(7)" indicates Equations (1)–(7) in Table 3.

4.3.2. Modeling of Multi-Mineral Saturation States

The multi-mineral equilibrium method used for geothermal systems represents a reservoir temperature calculation technique grounded on the simulation of multi-component chemical equilibrium in a geothermal system [50–54]. This method works on the principle that saturation indices (SIs) (SI = log(Q/K)) for an array of minerals synchronously converge to SI = 0 at a specific temperature [55]. Therein, Q denotes the ion activity product of the water sample, and K denotes the equilibrium constant (Reed) [53]. This temperature is identified as the fluid–mineral equilibrium temperature, which corresponds to the estimated reservoir temperature of a geothermal system [50].

In this study, the saturation indices of seven distinct minerals, namely dolomite, fluorite, quartz, chalcedony, calcite, gibbsite, and illite, at varying temperatures, were computed using the Phreeqc software (V 3.6) [56]. Subsequently, the log(Q/K) vs. T equilibrium diagrams for the water samples from the study area were constructed. The temperature intervals at which the curves of multiple minerals converge on the straight line with the vertical coordinate, log(Q/K) = 0, denote the temperatures of deep geothermal reservoirs.

An inspection of Figure 7 reveals that merely a minor segment of the mineral SI curves aligns with the straight line with the vertical coordinate, log(Q/K) = 0. The convergence temperature intervals appear rather dispersed, a phenomenon that is potentially attributed to the influence of cold water mixing occurring as the geothermal water ascends to the surface. Underground hot water undergoes modifications due to processes like precipitation, dissolution, and mixing during its ascent. Such alterations can result in an unbalanced appearance in the mineral SI curves [57]. Within this data set, the equilibrium diagrams for quartz, chalcedony, and calcite exhibited a more pronounced intersection with the straight line corresponding to the horizontal coordinate, log(Q/K) = 0. The reservoir temperature intervals determined by these intersections closely approach equilibrium. Furthermore, the Phreeqc software offers a limited temperature estimation range. Based on the findings presented in Figure 7 (these curves are optimized to fit the mineral data for each location), the reservoir temperature in the study area ranges between 80 and 140 °C.

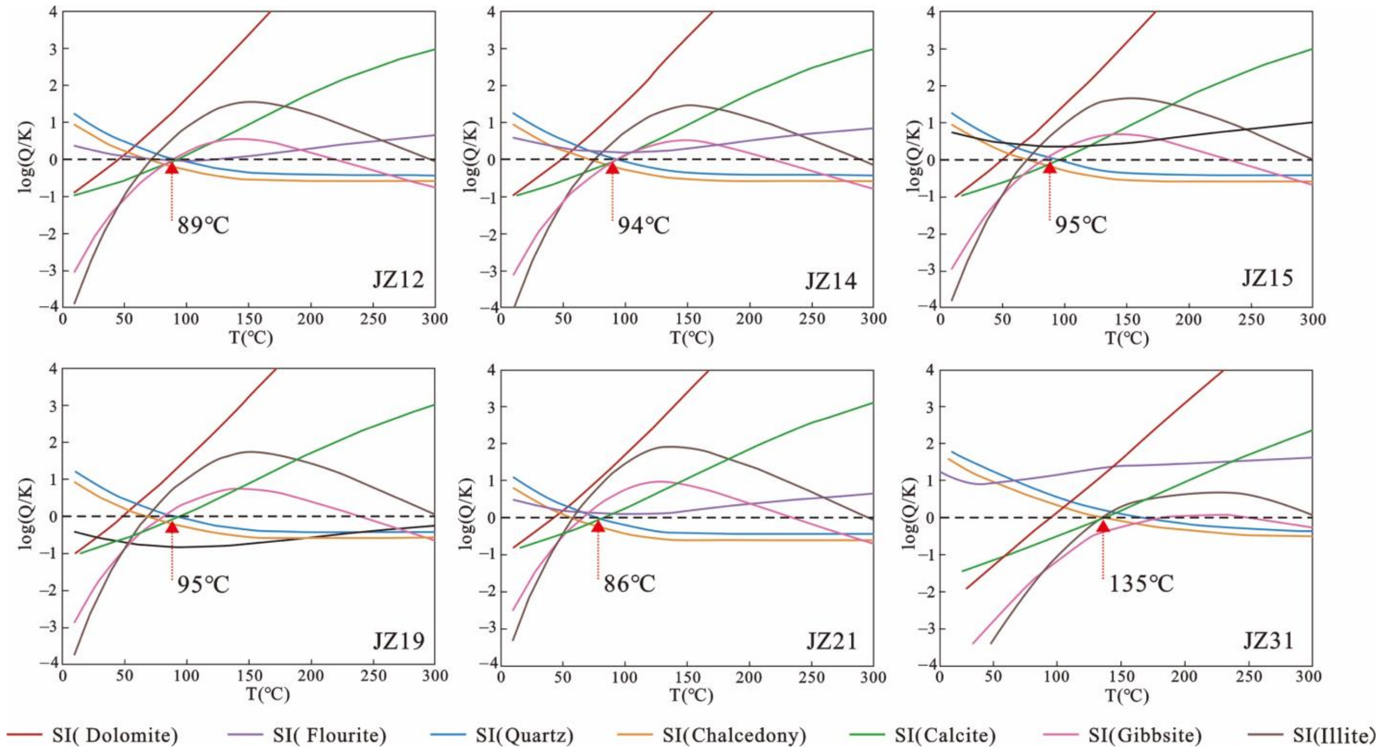

Figure 7. SI-T diagram of geothermal fluids in the study area.

4.3.3. Silica–Enthalpy Mixing Models

Fault development in the study area provides favorable runoff conditions, with the potential mixing of deep fluids with the near-surface cold water in the stage of geothermal water circulation. This study employed the silicon–enthalpy equation method [56,58,59] to analyze the hot water mixing conditions, constructing two distinct equations for the initial enthalpy of deep hot water [60]:

$$S_c X_1 + S_h(1 - X_1) = S_s \tag{8}$$

$$SiO_{2c}\mathrm{X}_2 + SiO_{2h}(1 - \mathrm{X}_2) = SiO_{2s} \tag{9}$$

where S_c is the enthalpy of the near-surface cold water, set at the local average annual temperature of 17.5 °C [20]; S_h denotes the initial enthalpy of the deep hot water; S_s is the final enthalpy of the hot water; SiO_{2c} represents the SiO_2 concentration in the near-surface cold water, established as 17.15 mg/L [20]; SiO_{2s} is the SiO_2 concentration in the deep hot water; and SiO_{2h} is the initial SiO_2 concentration in the deep hot water, and it is a function of S_h. X_1 is the proportion of mixed surface cold water with respect to enthalpy formation; X_2 is the proportion of mixed surface cold water with respect to SiO_2 content formation.

Substituting the specific enthalpies and the SiO_2 contents of underground hot water (Table 5) at designated temperatures in the study area into the equations yielded a series of X_1 and X_2 values (Table 6). Furthermore, the relationship between the hot water temperature and the cold water mixing ratio was plotted (Figure 8). The temperatures at the points of intersection between the X_1 and X_2 curves represent the highest reservoir temperatures before geothermal fluid mixing with cold water, as determined using the silicon–enthalpy equation method. As illustrated in Figure 8, the reservoir temperatures estimated using the silica–enthalpy equation method ranges from 100 °C to 150 °C.

Table 5. Relationship between temperature, enthalpy, and SiO_2 contents.

T (°C)	Enthalpy (×4.1868 J/g)	SiO_2 (mg/L)	T (°C)	Enthalpy (×4.1868 J/g)	SiO_2 (mg/L)
50	50	13.5	200	203.6	265
75	75	26.6	225	230.9	365
100	100.1	48	250	259.2	486
125	125.4	80	275	289	614
150	151	125	300	321	692
175	177	185			

(According to [56]).

Table 6. Results of X_1 and X_2 of the hot water.

T (°C)		50	75	100	125	150	175	200	225	250	275	300
X_1	JZ07	−0.52	0.14	0.40	0.54	0.63	0.70	0.75	0.79	0.83	0.86	0.90
	JZ09	−0.25	0.30	0.51	0.63	0.70	0.76	0.80	0.83	0.87	0.90	0.93
	JZ10	−0.75	0.01	0.31	0.47	0.58	0.65	0.71	0.75	0.80	0.84	0.87
	JZ23	−0.15	0.35	0.55	0.65	0.72	0.77	0.81	0.85	0.88	0.91	0.94
	JZ26	−0.10	0.38	0.57	0.67	0.74	0.79	0.82	0.86	0.89	0.92	0.95
	JZ31	−2.26	−0.84	−0.28	0.02	0.21	0.34	0.44	0.52	0.59	0.64	0.70
X_2	JZ07	13.23	−3.72	−0.45	0.29	0.59	0.73	0.82	0.87	0.90	0.93	0.93
	JZ09	13.62	−3.88	−0.49	0.27	0.57	0.70	0.81	0.87	0.90	0.92	0.93
	JZ10	16.48	−4.98	−0.83	0.10	0.48	0.64	0.77	0.84	0.88	0.91	0.92
	JZ23	9.14	−2.14	0.04	0.53	0.72	0.79	0.88	0.91	0.94	0.95	0.96
	JZ26	10.05	−2.50	−0.07	0.47	0.69	0.77	0.87	0.90	0.93	0.94	0.95
	JZ31	37.48	−13.09	−3.32	−1.12	−0.23	0.20	0.46	0.62	0.72	0.78	0.80

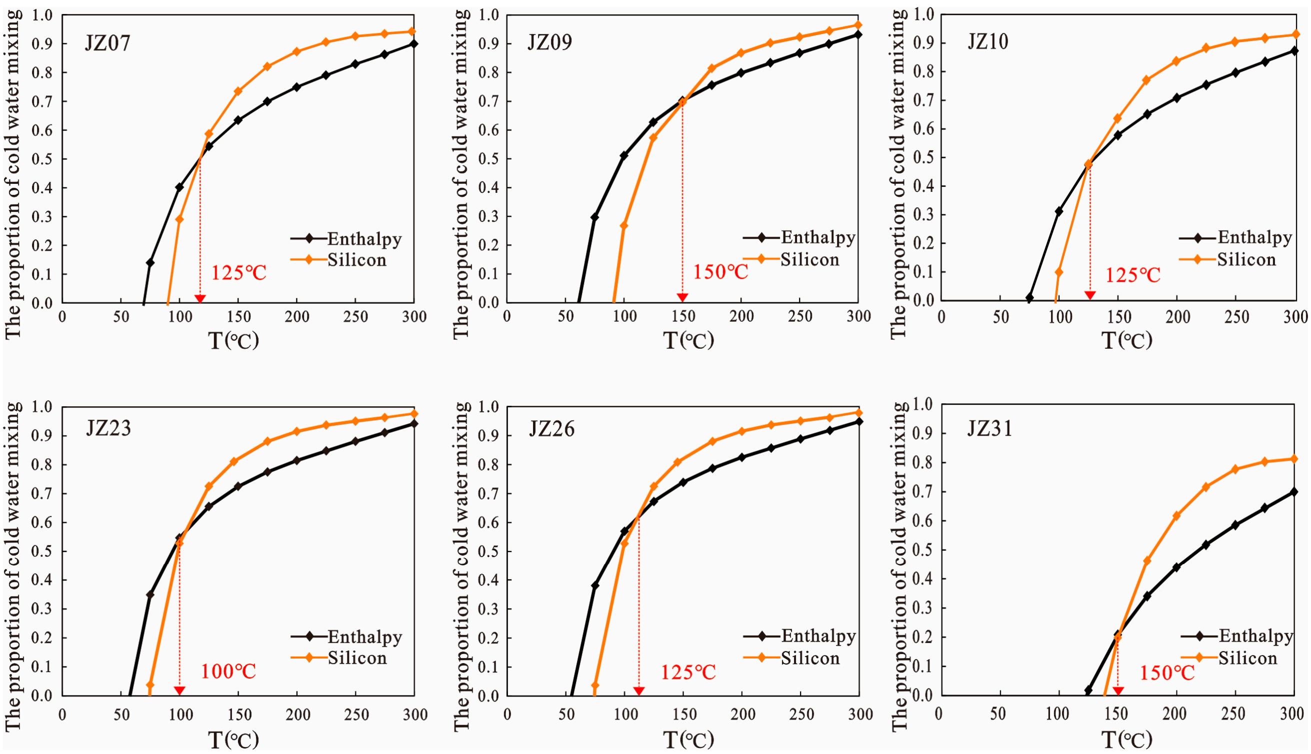

Figure 8. Silica–enthalpy mixing models of geothermal fluids in the study area.

This study estimated the deep reservoir temperature in the study area using the classical geothermometers, multi-mineral SI simulation, and the silicon–enthalpy equation method. The Si-enthalpy equation method operates under the ideal condition that no heat loss occurs in underground hot water prior to cold water mixing and takes into account the influence of cold water mixing on temperature reduction. However, the actual environment of deep geothermal reservoirs is more complex, and it is virtually impossible to achieve the ideal state. Furthermore, SiO_2 minerals, such as quartz, calcite, opal, and so on, are pervasive in natural rocks, and water-soluble SiO_2 is immune to common ionic effects, complex formation, and volatilization. Based on a thorough comparison of wellhead temperatures, geothermometers (Table 4), multiple mineral equilibrium diagrams, and the silicon–enthalpy equation method, it can be determined that the chalcedony geothermometer, which suggested deep reservoir temperatures ranging between 63 and 137.6 °C (Table 4), offered the most accurate estimation.

4.4. Circulation Depth

The Jizhong Depression, situated in the North China Plain, represents a sedimentary basin type of geothermal resources. In this region, the temperature of the underground hot water shows a positive correlation with the depth of thermal circulation. The following equation can be employed to approximate the depth of hot water circulation [61]:

$$H = \frac{t_1 - t_2}{I} + h \tag{10}$$

where H is the depth of hot water circulation; t_1 is the reservoir temperature (°C); t_2 is the multi-year average air temperature (°C); I is the geothermal gradient (°C/100 m); and h is the depth of the constant temperature zone (m). For the study area, the reservoir temperature was estimated from the results derived using a chalcedony geothermometer. Furthermore, the annual average temperature was set at 17.5 °C, the geothermal gradient was chosen as 3.5 °C/100 m [24], and the constant temperature zone depth was based on the regional value of 25 m [60]. Using these parameters, the thermal circulation depth for the deep geothermal reservoirs in the study area was estimated to range between 1324 m and 3455 m (Table 7).

Table 7. Estimation circulation depth of the hot water.

Sample No.	I/(°C/100 m)	t_1/°C	t_2/°C	h/m	H/m
JZ07	3.5	82.9	17.5	25	1979
JZ08	3.5	80.3	17.5	25	1820
JZ09	3.5	84.1	17.5	25	1928
JZ10	3.5	92.5	17.5	25	2167
JZ12	3.5	92.3	17.5	25	2162
JZ14	3.5	80.3	17.5	25	1820
JZ15	3.5	84.1	17.5	25	1928
JZ16	3.5	91.9	17.5	25	2151
JZ19	3.5	88.5	17.5	25	2053
JZ21	3.5	84.5	17.5	25	1939
JZ23	3.5	68.7	17.5	25	1488
JZ26	3.5	72.1	17.5	25	1586
JZ28	3.5	63.0	17.5	25	1324
JZ30	3.5	115.0	17.5	25	2811
JZ31	3.5	137.6	17.5	25	3455

5. Conceptual Genetic Model

The destruction of the North China Craton led to the thinned lithosphere and pronounced tectonic and thermal activity, facilitating the upward heat conduction from deeper sections. Carbonate rocks, possessing high thermal conductivity, refract this heat. Furthermore, heat flow migrates from depression zones with a low thermal conductivity to elevated areas with higher conductivity. By combining these mechanisms with favorable conditions, geothermal reservoirs that are abundant in deep geothermal resources are formed within the carbonate rock strata characterized by extensive karst fissures [62–64]. Based on the geochemical characteristics of thermal fluids in the geothermal reservoirs of ancient buried hills in the northern Jizhong Depression, as well as the geothermal geological conditions in the study area, this study established a conceptual model for the deep karst geothermal system; atmospheric precipitation in mountainous areas permeates through faults, journeying deep due to gravity. Over prolonged recharge via lateral runoff, this water enters the interior of the depression, fully absorbing significant heat from deeper sources. As a result, deep geothermal reservoirs form in the northern Jizhong Depression. Concurrently, regional tectonic faults offer optimal pathways for the transfer of deep water and heat sources. Furthermore, the deep groundwater circulation promotes the formation of geothermal anomalies (Figure 9).

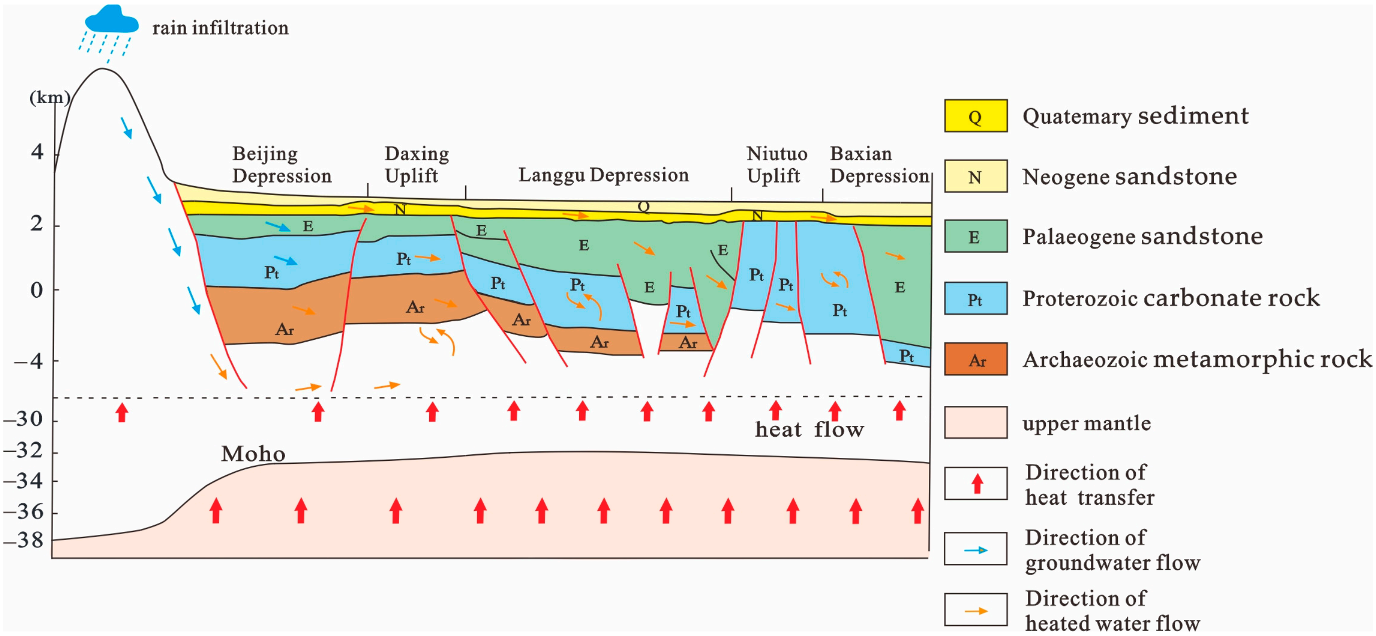

Figure 9. Distribution map of geothermal fluids in the study area [21,23].

6. Conclusions

The following conclusions can be drawn:

(1) Underground hot water samples from the deep carbonate geothermal reservoirs in the study area generally exhibit weak alkalinity. The total dissolved solids (TDS) in underground water increase progressively from the recharge area to the runoff area and finally to the discharge area. Concurrently, the hydrochemistry transitions from an oxidizing environment to a reducing environment. The primary recharge source for deep geothermal reservoirs is atmospheric precipitation in mountainous areas. As the depth of carbonate geothermal reservoirs increases, the environment becomes increasingly isolated, with intensified water–rock interactions and pronounced isotope exchange in warmer zones.

(2) The most suitable geothermometer for deep karst geothermal reservoirs in the study area is the chalcedony geothermometer. The estimated deep reservoir temperature ranges between 63 °C and 137.6 °C.

(3) Atmospheric precipitation in mountainous areas permeates through piedmont faults, journeying deep due to gravity. Regional tectonic faults provide favorable channels for the transfer of deep water and heat sources. Furthermore, deep groundwater circulation promotes the formation of geothermal anomalies.

Author Contributions: Conceptualization, M.Y. and X.T.; methodology, M.Y.; software, M.Y.; validation, M.Y., X.T. and H.Z.; formal analysis, M.Y.; investigation, M.Y., Z.Z., H.L. and X.Y.; resources, M.Y., X.T. and H.Z.; data curation, M.Y.; writing—original draft preparation, M.Y.; writing—review and editing, M.Y., X.T., H.Z., J.L., L.W., Z.Z., H.L. and X.Y.; visualization, X.Y.; supervision, H.Z.; project administration, X.T. and H.Z.; funding acquisition, X.T. and H.Z. All authors have read and agreed to the published version of the manuscript.

Funding: This research and APC were funded by the characteristics of geological environment endowment and the formation and evolution mechanism of environmental geological problems (grant number 225A4204D) and Comprehensive Evaluation and Layout Optimization of Bedrock Thermal Reserves in Hebei Plain (grant number 13000023P00329410174Y).

Data Availability Statement: All data analyzed in this study are available from the corre- sponding authors upon reasonable request.

Conflicts of Interest: Author Xinlong Yang was employed by the company Beijing Huaqing Geothermal Development Group Co., Ltd. The remaining authors declare that the research was conducted in the absence of any commercial or financial relationships that could be construed as a potential conflict of interest.

References

1. Tester, J.W.; Anderson, B.J.; Batchelor, A.S.; Blackwell, D.D.; Dipippo, R.; Drake, E.M. The Future of Geothermal Energy. *Mass. Inst. Technol.* **2006**, *358*, 1–3.
2. Hillis, R.R.; Hand, M.; Mildren, S.D.; Reid, P.D.; Reynolds, S.D.; Nelson, E.J. Hot Dry Rock Geothermal Exploration in Australia. *ASEG Ext. Abstr.* **2004**, *1*, 1–4. [CrossRef]
3. Wang, G.L.; Lin, W.J.; Zhang, W.; Lu, C.; Ma, F.; Gan, H.N. Research on Formation Mechanisms of Hot Dry Rock Resources in China. *Acta Geol. Sin.* **2016**, *90*, 1418–1433.
4. Liu, F.; Zhang, W.; Wang, G.L.; Wei, S.C.; Yue, C.; Jiang, G.Z.; Liao, Y.Z. Geothermal anomalies in the Xianshuihe area: Implications for tunnel construction along the Sichuan-Tibet Railway, China. *J. Groundw. Sci. Eng.* **2023**, *11*, 237–248. [CrossRef]
5. Shi, H.L.; Wang, G.L.; Lu, C. Numerical investigation on delaying thermal breakthrough by regulating reinjection fluid path in multi-aquifer geothermal system. *Appl. Therm. Eng.* **2022**, *221*, 119692. [CrossRef]
6. Lin, W.J.; Wang, G.; Gan, H.N.; Zhang, S.S.; Zhao, Z.; Yue, G.F.; Ting, L.X. Heat source model for Enhanced Geothermal Systems (EGS) under different geological conditions in China. *Gondwana Res.* **2023**, *122*, 243–259. [CrossRef]
7. Wang, G.L.; Lin, W.J. Main hydro-geothermal systems and their genetic models in China. *Acta Geol.* **2020**, *94*, 1923–1937. (In Chinese)
8. Ma, F.; Wang, G.L.; Zhang, W.; Zhu, X.; Zhang, H.X.; Yue, G.F. Structure of geothermal reservoirs and resource potential in the Rongcheng geothermal field in Xiong'an New Area. *Acta Geol. Sin.* **2020**, *94*, 1981–1990. (In Chinese)
9. Wang, G.L.; Zhang, W.; Liang, J.Y.; Lin, W.J.; Liu, Z.M.; Wang, W.L. Evaluation of Geothermal Resources Potential in China. *Acta Geosci. Sin.* **2017**, *38*, 12. (In Chinese)
10. Li, M.; Xing, L.X.; Wang, G.L.; Zhang, W.; Zhao, J.Y.; Jin, M.G. Distribution characteristics of fluorine in deep geothermal water in Jizhong Depression and its risk assessment and suggestions for utilization. *Geol. China* **2023**. (In Chinese)
11. Eberhard, L.; Pettke, T. Antigorite dehydration fluids boost carbonate mobilisation and crustal CO_2 outgassing in collisional orogens. *Geochim. Cosmochim. Acta* **2021**, *300*, 192–214. [CrossRef]
12. Weydt, L.M.; Heldmann, C.D.J.; Machel, H.G.; Sass, I. From oil field to geothermal reservoir: Assessment for geothermal utilization of two regionally extensive Devonian carbonate aquifers in Alberta, Canada. *Solid Earth* **2018**, *9*, 953–983. [CrossRef]
13. Hoefs, J. *Stable Isotope Geochemistry/Jochen Hoefs*; Springer: Berlin/Heidelberg, Germany, 2009.
14. Chimeddorj, B.; Munkhbat, D.; Altanbaatar, B.; Dolgorjav, O.; Oyuntsetseg, B. Hydrogeochemical characteristics and geothermometry of hot springs in the Altai region, Mongolia. *Geochem. Explor. Environ. Anal.* **2021**, *21*, 4. [CrossRef]
15. Stober, I.; Bucher, K. *Geothermal Energy: From Theoretical Models to Exploration and Development*; Springer Nature: Basel, Switzerland, 2021.
16. Yurteri, C.; Simsek, S. Hydrogeological and hydrochemical studies of the Kaman-Savcili-Büyükoba (Kirsehir) geothermal area, Turkey. *Geothermics* **2017**, *65*, 99–112. [CrossRef]
17. Soldatova, E.A.; Guseva, N.V.; Sun, Z.; Mazurova, I.S. Size fractionation of trace elements in the surface water and groundwater of the Ganjiang River and Xiushui River basins, China. *IOP Conf. Ser. Earth Environ. Sci.* **2015**, *27*, 012037. [CrossRef]
18. Han, D.M.; Currell, M.J. Delineating multiple salinization processes in a coastal plain aquifer, northern China: Hydrochemical and isotopic evidence. *Hydrol. Earth Syst. Sci.* **2018**, *22*, 3473–3491. [CrossRef]

19. Pang, J.M.; Pang, Z.H.; Lv, M.; Tian, J.; Kong, Y.L. Geochemical and isotopic characteristics of fluids in the Niutuozhen geothermal field, North China. *Environ. Earth Sci.* **2018**, *77*, 12. [CrossRef]
20. Zhu, X.; Wang, G.L.; Wang, X.Y.; Qi, S.H.; Ma, F.; Zhang, W.; Zhang, H.X. Hydrogeochemical and Isotopic Analyses of Deep Geothermal Fluids in the Wumishan Formation in Xiong'an New Area, China. *Lithosphere* **2022**, *2022*, 2576752. [CrossRef]
21. Yu, M.X.; Wang, G.L.; Ma, F.; Zhang, W.; Lin, W.J.; Zhu, X.; Zhang, H.X. Geochemical characteristics of geothermal fluids of a deep ancient buried hill in the Xiong'an New Area of China. *Water* **2022**, *14*, 3182. [CrossRef]
22. Wang, Y.J.; Ma, F.; Xie, H.P.; Wang, G.L.; Wang, Z.H. Fracture Characteristics and Heat Accumulation of Jixianian Carbonate Reservoirs in the Rongcheng Geothermal Field, Xiong'an New Area. *Acta Geol. Sin. Engl. Ed.* **2021**, *95*, 1902–1914. [CrossRef]
23. He, D.F.; Cui, Y.Q.; Shan, S.Q.; Xiao, Y.; Zhang, Y.Y.; Zhang, C.B. Characteristics of geologic framework of buried-hill in Jizhong depression, Bohai Bay Basin. *Chin. J. Geol.* **2018**, *53*, 1–24. (In Chinese)
24. Chang, J.; Qiu, N.S.; Zhao, X.Z.; Xu, W.; Xu, Q.C.; Jin, F.M.; Han, C.Y.; Ma, X.F.; Dong, X.Y. Present-day geothermal regime of the Jizhong depression in Bohai Bay basin, East China. *Chin. J. Geophys.* **2016**, *59*, 1003–1016. (In Chinese)
25. Zhao, H.G.; Liu, C.Y. Research on the Segmentation of Daxing Fault. *Oil Cas Geol.* **2002**, *23*, 368–371. (In Chinese)
26. Zhao, J.Y.; Zhang, W.; Ma, F.; Zhu, X.; Zhang, H.X.; Wang, G.L. Geothemical characteristics of the geothermal fluid in the Rongcheng geothermal field, Xiong'an New Area. *Acta Geol. Sin.* **2020**, *94*, 1992–2001. (In Chinese)
27. Zhu, X.; Wang, G.L.; Ma, F.; Lin, W.J.; Zhang, W.; Zhang, B.J.; Jia, X.F.; Zhang, H.X. Evaluation of Geothermal Resources of the Xiong'an New Area. *Earth Sci.* **2023**, *48*, 1093–1106. (In Chinese)
28. Song, J.J.; Wang, G.L.; Xing, L.X.; Qian, J.Z.; Dai, L.; Di, H. Influencing factors of rock thermal conductivity and applicability ecaluation of its mixing law predicitive models. *Geothermics* **2023**, *110*, 102680. [CrossRef]
29. Yang, M.H.; Liu, C.Y.; Sun, D.S.; Cui, Y.Q. Extensional tectonic system and its deep-seated setting of Jizhong Basin, China. *Geotectinic Metallog.* **2002**, *26*, 113–120. (In Chinese)
30. *DZ/T 0184.6-1997*; Determination of Samarium-Neodymium Isotope Geological Age and Neodymium Isotope Ratio. Institute of Geology, Ministry of Geology and Mineral Resources: Nanjing, China, 1997. (In Chinese)
31. Deng, J.Z. Chemical Characteristics and Genetic Analysis If Geothermal Water in Carbonate Reservoir in the Northern Jizhong Depression. Master's Thesis, East China University of Technology, Shanghai, China, 2022. (In Chinese).
32. Mazela, W.; Krasodomski, W.; Pajda, M. Assessment of the Main Threats to Injection Well Damage Caused by Reservoir Waters using AquaChem Software as well as Laboratory Tests Application. *J. China Hydrol.* **2012**, *29*, 50–53.
33. Dinka, M.O.; Loiskandl, W.; Ndambuki, J.M. Hydrochemical characterization of various surface water and groundwater resources available in Matahara areas, Fantalle Woreda of Oromiya region. *J. Hydrol. Reg. Stud.* **2015**, *3*, 444–456. [CrossRef]
34. Arnórsson, S. *Isotopic and Chemical Techniques in Geothermal Exploration, Development and Use*; International Atomic Energy Agency: Vienna, Austria, 2000; p. 351.
35. Liu, M.L.; He, T.; Wu, Q.F.; Guo, Q.H. Hydrogeochemistry of geothermal waters from Xiong'an New Area and its Indicating significance. *Earth Sci.* **2020**, *45*, 2221–2231. (In Chinese)
36. *GB8537-2018*; National Standard for Food Safety Drinking Natural Mineral Water. National Health Commission of the People's Republic of China State Administration for Market Regulation: Beijing, China, 2018. (In Chinese)
37. Wang, S.Q.; Zhang, B.J.; Yan, L.Y.; Xing, Y.F.; Yuan, W.Z.; Li, J.; Gao, J.; Zhao, T. Heat accumulation mechanism of deep ancient buried hill in the northeast of Gaoyang geothermal field, Xiong'an New Area. *Bull. Geol. Sci. Technol.* **2021**, *40*, 12–21. (In Chinese)
38. Can, I. A new improved Na/K geothermometer by artificial neural networks. *Geothermics* **2002**, *31*, 751–760. [CrossRef]
39. Henley, R.W.; Truesdell, A.H.; Barton, P.B., Jr.; Whitney, J.A. Fluid-Mineral Equilibria in Hydrothermal Systems. *Soc. Econ. Geol.* **1984**, *1*, 66.
40. Deng, J.Z.; Lin, W.J.; Xing, L.X.; Chen, L. The Estimation of Geothermal Reservoir Temperature Based on Integrated Multicomponent Geothermometry: A Case Study in the Jizhong Depression, North China Plain. *Water* **2022**, *14*, 2489. [CrossRef]
41. Pang, Z.H.; Kong, Y.L.; Pang, J.M.; Hu, S.B.; Wang, J.Y. Geothermal resources and development in Xiong'an New Area. *Bull. Chin. Acad. Sci.* **2017**, *32*, 1224–1230. (In Chinese)
42. Jiang, Y.; Li, J.; Xing, Y.F.; Liu, Y.L.; Wang, H.Q.; Teng, Y.G.; Wang, G.L. Evaluation of Geochemical Geothermometers with Borehole Geothermal Measurements: A Case study of the Xiong'an New Area. *Earth Sci.* **2023**, *48*, 958–972. (In Chinese)
43. Fournier, R.O. Chemical geothermometers and mixing models for geothermal systems. *Geothermics* **1977**, *5*, 41–50. [CrossRef]
44. Fournier, R.O.; Rowe, J.J. Estimation of underground temperatures from the silica content of water from hot springs and wet-steam wells. *Am. J. Sci.* **1966**, *264*, 685–697. [CrossRef]
45. Fournier, R.O.; Truesdell, A.H. An empirical Na-K-Ca geothermometer for natural waters. *Geochim. Cosmochim. Acta* **1973**, *37*, 1255–1275. [CrossRef]
46. Fournier, R.O.; Truesdell, A.H. Geochemical indicators of subsurface temperature: Part 2, estimation of temperature and fraction of hot water mixed with cold water. *J. Res. US Geol. Surv.* **1974**, *2*, 263–270.
47. Giggenbach, W.F. Geothermal solute equilibria. Derivation of Na-K-Mg-Ca geoindicators. *Geochim. Cosmochim. Acta* **1988**, *52*, 2749–2765. [CrossRef]
48. Li, J.X. Study on the Key Factors of Geothermometers and Their Application: A Case Study of Crystalline Basement Reservoirs. Ph.D. Thesis, China University of Geosciences, Wuhan, China, 2019. (In Chinese).
49. Wei, Z.A.; Huang, S.P.; Wang, C.S.; Zhang, M. Geochemistry and Its Geothermal Reservoir Implications of Geothermal Water in the Guangdong-Hong Kong-Macao Greater Bay Area, South China. *Acta Geosci. Sin.* **2023**, *44*, 117–132. (In Chinese)

50. Benjamin, T.; Charles, R.; Vidale, R. Thermodynamic parameters and experimental data for the Na-K-Ca geothermometer. *J. Volcanol. Geotherm. Res.* **1983**, *15*, 167–186. [CrossRef]
51. Chiodini, G.; Cioni, R.; Guidi, M.; Marini, L. Chemical geothermometry and geobarometry in hydrothermal aqueous solutions: A theoretical investigation based on a mineral-solution equilibrium model. *Geochim. Cosmochim. Acta* **1991**, *55*, 2709–2727. [CrossRef]
52. Alsemgeest, J.; Auqué, L.F.; Gimeno, M.J. Verification and comparison of two thermodynamic databases through conversion to PHREEQC and multicomponent geothermometrical calculations. *Geothermics* **2021**, *91*, 102036. [CrossRef]
53. Reed, M.; Spycher, N. Calculation of pH and mineral equilibria in hydrothermal water with application to geothermometry and studies of boiling and Dilution. *Geochim. Cosmochim. Acta* **1984**, *48*, 1479–1492. [CrossRef]
54. Spycher, N.; Peiffer, L.; Sonnenthal, E.L.; Saldi, G.; Reed, M.H.; Kennedy, B.M. Integrated multicomponent solute geothermometry. *Geothermics* **2014**, *51*, 113–123. [CrossRef]
55. Tole, M.P.; Ármannsson, H.; Zhong-He, P.; Arnórsson, S. Fluid/mineral equilibrium calculations for geothermal fluids and chemical geothermometry. *Geothermics* **1993**, *22*, 17–37. [CrossRef]
56. Parkhurst, D.L.; Appelo, C.A.J. User's Guide to PHREEQC (Version 2)—A Computer Program for Speciation, Batch-Reaction, One-Dimensional Transport, and Inverse Geochemical Calculations. *Water Resour. Investig. Rep.* **1999**, *99*, 1–317.
57. Xu, W.C. Application of the saturation index method to the study of geothermal geochemistry. *J. Xi'an Coll. Geol.* **1992**, *14*, 66–70. (In Chinese)
58. Truesdell, A.H.; Fournier, R.O. Procedure for estimating the temperature of a hot-water component in a mixed water by using a plot of dissolved silica versus enthalpy. *J. Res. U.S. Geol. Surv* **1977**, *5*, 49–52.
59. Keenan, J.H.; Keyes, F.G.; Hill, P.G.; Moore, J.G. *Steam Tables-Thermodynamic Properties of Water Including Vapor, Liquid, and Solid Phases (International Edition—Metric Units)*; Wiley: Hoboken, NJ, USA, 1969.
60. Zhao, Z.R.; Zhang, W.; Wang, G.L.; Xing, L.X.; Zhang, H.X.; Zhao, J.Y. Hydrogeochemical characteristics of Gaoyang geothermal field in central Hebei Depression and its constraint on geothermal genesis. *Geol. China* **2023**. (In Chinese)
61. Zhang, W.; Wang, G.L.; Zhao, J.Y.; Liu, F. Geochemical characteristics of medium-high temperature geothermal fluids in West Sichuan and their geological implications. *Geoscience* **2021**, *35*, 188–198. (In Chinese)
62. Yu, M.X.; Ma, F.; Wang, G.L.; Zhang, W.; Zhu, X.; Zhang, H.X.; Wang, Y.X. Characteristics and Evaluation of Geothermal Resources in the Rongdong Area of Xiong'an New Area. *Acta Geosci. Sin.* **2023**, *44*, 180–190. (In Chinese)
63. Shahbaz, A.M.; Nakashima, Y.; Nishigaki, M. Clogging mechanisms and preventive measures in artificial recharge systems. *J. Groundw. Sci. Eng.* **2021**, *9*, 181–201.
64. Mohammad, A.T.; Jalut, Q.H.; Abbas, N.L. Predicting groundwater level of wells in the Diyala River Basin in eastern Iraq using artificial neural network. *J. Groundw. Sci. Eng.* **2020**, *8*, 87–96.